Numerical modeling of carbon/carbon composites with nanotextured matrix and 3D pores of irregular shapes

B. Drach, I. Tsukrov, T. Gross, S. Dietrich, Kay A. Weidenmann, R. Piat, T. Böhlke

Angaben zur Veröffentlichung / Publication details:

Drach, B., I. Tsukrov, T. Gross, S. Dietrich, Kay A. Weidenmann, R. Piat, and T. Böhlke. 2011. "Numerical modeling of carbon/carbon composites with nanotextured matrix and 3D pores of irregular shapes." *International Journal of Solids and Structures* 48 (18): 2447–57. https://doi.org/10.1016/j.ijsolstr.2011.04.021.

Numerical modeling of carbon/carbon composites with nanotextured matrix and 3D pores of irregular shapes

B. Drach [a], I. Tsukrov [a,*], T. Gross [a], S. Dietrich [b], K. Weidenmann [b], R. Piat [b], T. Böhlke [b]

[a] University of New Hampshire, Durham, NH 03824, USA
[b] Karlsruhe Institute of Technology, Karlsruhe, Germany

1. Introduction

In this paper, we propose a computational procedure to determine the effective elastic properties of porous nanotextured pyrolytic carbon (PyC). This material is an important constituent of many high performance material systems including carbon/carbon composites used in the aerospace industry for heat shielding and brake pads in commercial aircrafts.

For these applications, the material is produced by chemical vapor infiltration (CVI) of fiber preforms or chemical vapor deposition on flat substrates. The resulting microstructure is characterized by the presence of irregularly shaped pores and varying degree of nanotexture in the PyC.

One of the challenges in predicting the overall elastic behavior of pyrolytic carbon is that its degree of organization and mechanical properties are determined by the manufacturing parameters as well as by the topology and composition of the substrate. When the material is produced by CVI, the manufacturing parameters include temperature, pressure, residence time and the choice of precursor gas. It has been shown that variations in these parameters may result in isotropic, low-, medium- or high-textured PyC (Reznik and Hüttinger, 2002; López-Honorato et al., 2010). The level of texture can also change with the distance from the substrate (Reznik et al., 2003; Piat et al., 2008).

* Corresponding author. Address: Kingsbury Hall, W101, 33 Academic Way, Durham, NH 03824, USA. Tel.: +1 (603) 862 2086; fax: +1 (603) 862 1865.
E-mail address: igor.tsukrov@unh.edu (I. Tsukrov).

Fig. 1 illustrates different methods used to characterize the nanotexture of PyC. A schematic representation of one fiber (F), surrounded by layers of PyC is shown in Fig. 1a. Polarized light microscopy (PLM) of the material on the scale of tens of microns allows characterization of the level of texture orientation by the extinction angle (Fig. 1b), see Bortchagovsky et al. (2003) and Gray and Cathcart (1966). Transmission electron microscopy (Fig. 1c) with segmentation analysis or selected area electron diffraction (SAED) technique (an example of an anisotropic diffraction pattern is shown in Fig. 1d) can be used to resolve the spatial distribution of nanotexture orientation on the scale of tens of nanometers, see Lin et al. (2010) and Reznik and Hüttinger (2002) for detailed information on the methods.

Overall mechanical behavior of porous materials is influenced not only by the volume fraction of pores (porosity) but also by their shape and distribution. Fig. 2 presents an example of C/C composite characterized by X-ray computed microtomography as described in Section 4.1. The pores in the material appear to be distributed randomly and have highly irregular shapes. Traditional approaches to evaluate the contributions of pores to effective elastic properties are based on the Eshelby solution for ellipsoidal shapes (Eshelby, 1957, 1959; Mura, 1987). However, due to the irregularity of pore geometry, such approaches are not suitable in this case.

The choice of available results for irregular pore shapes is quite limited. For 2D geometries, the solutions based on conformal mapping were utilized by Zimmerman (1986, 1991b), Kachanov et al. (1994), Jasiuk et al. (1994), Tsukrov and Novak (2002),

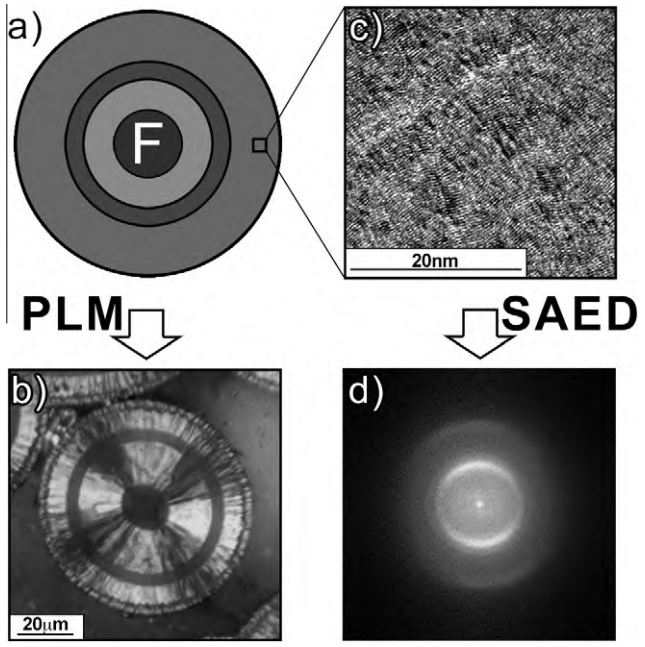

Fig. 1. Characterization of the nanotexture by polarized light microscopy (PLM) and selected area electron diffraction (SAED).

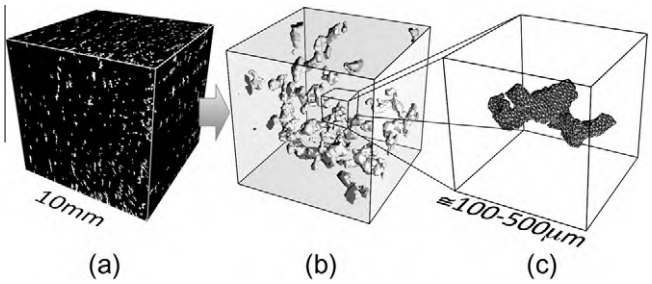

Fig. 2. Processing of microtomography (μCT) data: (a) series of black and white images, (b) extracted pore surfaces, and (c) finite element mesh from the pore surface.

Ekneligoda and Zimmerman (2006, 2008), and Zou et al. (2010). Numerical techniques can also be used to predict effective mechanical properties of 2D materials with non-elliptical pores, see, for example, Ekneligoda and Zimmerman (2007).

For 3D inhomogeneities, analytical solutions for non-ellipsoidal shapes can be found in Faivre (1964), Lee and Johnson (1978), Wu and Du (1995), Rodin (1996), Markenscoff (1998), Nozaki and Taya (1997, 2001). The results for cavities can be obtained from these solutions either by assuming the inhomogeneity stiffness to be zero, or by applying a limiting procedure for stiffness approaching zero. The relation between compliances of inhomogeneities having the same (regular or irregular) shape but different elastic constants is discussed in Sevostianov and Kachanov (2007), an example of finite element analysis (FEA) calculation and subsequent analysis for a "generalized ellipsoid" is given in Sevostianov et al. (2008). Another commonly used technique involves FEA of a representative volume element filled with a sufficient number of inhomogeneities, see, for example, Arns et al. (2002), Böhm et al. (2004), González et al. (2004) and later publications by these research groups.

Our approach to micromechanical modeling of materials with irregularly shaped 3D pores combines numerical and analytical techniques. The compliance contribution tensor of individual pores is found by FEA as described in Section 4.2 (note that there are no constraints on the level of anisotropy of the matrix material). This tensor is then incorporated in the micromechanical procedure presented in Section 3. The results for an isotropic matrix material with irregularly shaped pores are presented in Section 5.1. The case in which pores are present in a unidirectional C/C composite (transversely isotropic material) is given in Section 6.

2. Elastic properties of PyC with axisymmetric textures

PyC can be considered an assemblage of submicron transversely isotropic domains consisting of aligned graphene planes. Predictions of its effective elastic properties by traditional homogenization techniques, e.g. first order bounds, are rather inaccurate due to high domain anisotropy. In this section, we outline a more precise estimate, namely the singular approximation (Fokin, 1972, 1973; Böhlke et al., 2010). The essential feature of the singular approximation is the fact that the nonlocal part of the integral operator determining the strain field based on the stress polarization field is neglected. As a result, morphologic anisotropies cannot be taken into account by the singular approximation, i.e. isotropic two-point statistics are assumed. Since TEM images show approximately spherical domains on the submicron scale, this homogenization scheme seems to be appropriate. A specific property of the singular approximation is its self-consistency in the sense that the homogenized stiffness is inverse to the homogenized compliance.

To determine the singular approximation, three different data sets are required: the elastic constants of the transversely isotropic elastic domains, the stiffness tensor of the comparison material, and the orientation distribution function of the domains. The following elastic constants are taken for the domains: $C_{1111} = 40$ GPa, $C_{3333} = 18.2$ GPa, $C_{1122} = 20$ GPa, $C_{1133} = 13$ GPa, $C_{2323} = 1.8$ GPa, which were determined by ultrasound phase spectroscopy for a highly textured PyC sample (Gebert et al., 2010).

The comparison material required for the singular approximation is specified by the isotropic geometric mean (Böhlke et al., 2010) of the domain properties.

The orientation distribution of domains can be modeled based on a one-parameter axial orientation distribution function. According to the central limit theorem, any finite sum of independent and identically distributed random numbers in Euclidean space can be approximated by a Gaussian distribution. No simple analogue for the central limit theorem for hyperspheres exists. However, for the purpose of mathematical statistics, an analogue of the Gauss normal distribution for hyperspheres is the von-Mises-Fisher distributions. The von-Mises-Fisher distribution depends on two parameters: the expectation value of the c-axis of the domains and the concentration parameter κ, which is an analogue to the standard deviation of Gauss normal distributions. For a concentration parameter equal to zero the distribution is uniform, i.e. isotropic. Due to the rotational symmetry of the von-Mises-Fisher distribution, the effective response of the micro textured volume element is also one of transversely isotropic symmetry. Details of the discretization of the continuous von-Mises-Fisher distribution can be found in Böhlke et al. (2010).

Böhlke et al. (2010), shows that there is a significant gap between the first-order bounds, which implies that these bounds are not appropriate for estimating the effective properties. In the range between the bounds, morphologic aspects of the microstructure determine the precise values of the effective properties. Furthermore, it has been shown that the singular approximation is very close to the self-consistent estimate. The singular approximation is much simpler to determine and therefore preferable in this case.

Three specific orientation distributions of domains are considered in this paper: $\kappa = 0$ (isotropic overall material behavior),

$\kappa = 0.1$ (typical low texture PyC), and $\kappa = 100$ (high texture PyC). The components of the corresponding PyC stiffness tensors are given in Sections 5.1 and 6.

3. Contribution of pores to overall elastic properties

One of the approaches to characterize contribution of irregularly shaped pores to the effective elastic properties of PyC is based on the evaluation of their compliance and stiffness contribution tensors (Kachanov et al., 1994, 2003; Sevostianov and Kachanov, 2002;Tsukrov and Novak, 2002;Eroshkin and Tsukrov, 2005).

The approach is based on the concept of a representative volume element (RVE) (Hill, 1963; Nemat-Nasser and Hori, 1993). The presence of inhomogeneities in the RVE results in additional strains $\Delta\boldsymbol{\varepsilon}$ (stresses $\Delta\boldsymbol{\sigma}$) related to the externally applied homogeneous stresses $\boldsymbol{\sigma}_0$ (strains $\boldsymbol{\varepsilon}_0$) as

$$\Delta\boldsymbol{\varepsilon} = H_{RVE} : \boldsymbol{\sigma}_0, \quad \Delta\boldsymbol{\sigma} = N_{RVE} : \boldsymbol{\varepsilon}_0 \tag{3.1}$$

where H_{RVE} and N_{RVE} correspond to the compliance and stiffness contribution tensors (Kachanov et al., 1994, 2003). The effective compliance and stiffness of the entire composite are expressed in terms of these tensors as

$$\mathbf{S} = \mathbf{S}_0 + H_{RVE}, \quad \mathbf{C} = \mathbf{C}_0 + N_{RVE} \tag{3.2}$$

where $\mathbf{S}_0$ and $\mathbf{C}_0$ are the compliance and stiffness of a matrix material.

The exact values for components of H and N are found by direct solution of the boundary value problem for an RVE with all interacting inhomogeneities. Such solutions are usually not obtainable analytically, while numerical solutions require significant computational effort (and often involve statistical processing of the data obtained on particular implementations of microstructure).

To perform homogenization analytically, several micromechanical schemes have been developed. Their implementation in terms of H_{RVE} is discussed in Eroshkin and Tsukrov (2005) and is based on the compliance contribution tensors of individual inhomogeneities. If inhomogeneities are sufficiently far away from each other (dilute limit), the non-interaction approximation can be used. In this case, the corresponding contribution tensors are obtained by direct summation:

$$H^{NI}_{RVE} = \sum H^{(i)}, \quad N^{NI}_{RVE} = \sum N^{(i)} \tag{3.3}$$

where $H^{(i)}$ and $N^{(i)}$ are the compliance and stiffness contribution tensors of individual inhomogeneities, and the summation is performed over all defects present in the RVE. Note that H_{RVE} and N_{RVE} (as well as $H^{(i)}$ and $N^{(i)}$) possess the symmetry of elasticity tensor, so that

$$H_{ijkl} = H_{jikl} = H_{ijlk} = H_{klij}, \quad N_{ijkl} = N_{jikl} = N_{ijlk} = N_{klij} \tag{3.4}$$

As shown in Eroshkin and Tsukrov (2005), the predictions of more advanced micromechanical schemes can be readily obtained when the non-interaction approximation is known. For example, predictions for the overall elastic compliance by the Mori–Tanaka method (Mori and Tanaka, 1973; Benveniste, 1987) is given by

$$\mathbf{S} = \mathbf{S}_0 + H^{MT}_{RVE}, \quad H^{MT}_{RVE} = H^{NI}_{RVE} : \left[p(\mathbf{S}_I - \mathbf{S}_0) + H^{NI}_{RVE}\right]^{-1} : (\mathbf{S}_I - \mathbf{S}_0) \tag{3.5}$$

where p is the volume fraction of inhomogeneities and $\mathbf{S}_I$ is their compliance tensor. For the pores, the limiting procedure results in $H^{MT}_{RVE} = H^{NI}_{RVE}/(1-p)$ (see Kachanov et al., 1994).

In the case of regular pore shapes, the elasticity problem for a single pore can be solved analytically and explicit expressions for H and N tensors can be found. For the irregular pore shapes observed in C/C composites, the compliance and stiffness contribution tensors can be calculated by FEA as presented in Section 4.2.

4. Microtomography data processing and FEA analysis procedure

4.1. X-ray computed microtomography data acquisition and processing

The three dimensional distribution of pores was determined using X-ray computed microtomography (μCT). μCT is a non-destructive method for obtaining detailed 3D representation of material microstructure (see, for example, Salvo et al., 2003; Gebert et al., 2008). The method is based on measuring attenuation of X-rays passing through a material. The level of attenuation depends on the atomic masses of material constituents, so information on their shape and location can be obtained.

The microtomographic studies were performed in the Institute of Materials Science and Engineering I, Karlsruhe Institute of Technology, Germany. The analyzed cubic $1 \times 1 \times 1$ cm specimen was cut from CVI infiltrated C/C laminate using high speed water cutting and examined in a desktop CT scanner Skyscan 1072 with a voxel edge length of 14.7 μm, overall image size of 680^3 voxels and a dynamic gray value range of 16 bit. The C/C laminate consisted of four unidirectional C/C composite layers ($[0°/90°]_2$) of 2.3 mm thickness each, separated by 0.4 mm thick layers of chemical vapor infiltrated random felt.

Prior to the evaluation of single pores the image was subjected to multiple data processing steps implemented using ITK and VTK libraries (Ibanez et al., 2005). First, the image was filtered using a 3D anisotropic Gaussian filter, which allowed for an edge-preserving filtering without smearing the geometrical properties of the pores. Following this step, a connected component region growing algorithm was used to binarize the image. The parameters of the binarization process were adjusted to provide optimal correspondence with the manually classified binarizations of several pores.

The resulting sequence of black and white images was imported into open source software ParaView 3.6.2 (www.paraview.org), where it was converted into 3D surfaces for the separation of individual cavities and exported to stereolithography (STL) format. The triangulated surfaces of pores from the corresponding STL files were then used to create tetrahedral mesh for finite element analysis.

4.2. Evaluation of contribution of a single pore by finite element analysis

Pore compliance contribution tensor H of an individual pore was calculated numerically using FEA with MARC 2008 software package (www.mscsoftware.com). The following procedure was used:

(a) The pore surface mesh (extracted from X-ray computed microtomography data as described in Section 4.1) was placed into a cube-shaped reference volume with sides five times larger than the largest dimension of the pore (Fig. 3). This setup was auto meshed with tetrahedral 3D elements (#134 using MARC classification). Typical pore shapes yield FE meshes with the number of elements on the order of 100,000;

(b) Boundary conditions were applied in displacements for convenience of pre-processing. To obtain all 21 independent components of H-tensor, the following six loadcases were considered:

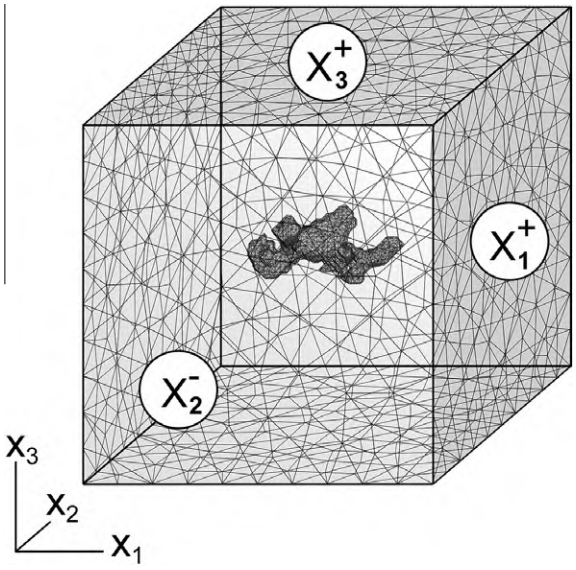

Fig. 3. Reference volume, pore surface mesh and coordinate plane notation.

Loadcase 1 (uniaxial tension in x_1 direction):

$$X_1^- : u_1 = 0; \quad X_1^+ : u_1 = \varepsilon^{(0)} \cdot a;$$
$$X_1^-, X_1^+, X_2^-, X_2^+, X_3^-, X_3^+ : u_2 = 0; \quad u_3 = 0;$$

Loadcase 2 (uniaxial tension in x_2 direction):

$$X_2^- : u_2 = 0; \quad X_2^+ : u_2 = \varepsilon^{(0)} \cdot a;$$
$$X_1^-, X_1^+, X_2^-, X_2^+, X_3^-, X_3^+ : u_1 = 0; \quad u_3 = 0;$$

Loadcase 3 (uniaxial tension in x_3 direction):

$$X_3^- : u_3 = 0; \quad X_3^+ : u_3 = \varepsilon^{(0)} \cdot a;$$
$$X_1^-, X_1^+, X_2^-, X_2^+, X_3^-, X_3^+ : u_1 = 0; \quad u_2 = 0;$$

Loadcase 4 (shear deformation in x_1x_2 plane):

$$X_1^- : u_2 = 0; \quad X_1^+ : u_2 = \varepsilon^{(0)} \cdot a;$$
$$X_1^-, X_1^+, X_2^-, X_2^+, X_3^-, X_3^+ : u_1 = 0; \quad u_3 = 0;$$

Loadcase 5 (shear deformation in x_2x_3 plane):

$$X_2^- : u_3 = 0; \quad X_2^+ : u_3 = \varepsilon^{(0)} \cdot a;$$
$$X_1^-, X_1^+, X_2^-, X_2^+, X_3^-, X_3^+ : u_1 = 0; \quad u_2 = 0;$$

Loadcase 6 (shear deformation in x_3x_1 plane):

$$X_3^- : u_1 = 0; \quad X_3^+ : u_1 = \varepsilon^{(0)} \cdot a;$$
$$X_1^-, X_1^+, X_2^-, X_2^+, X_3^-, X_3^+ : u_2 = 0; \quad u_3 = 0;$$

where $X_1^+, X_1^-, X_2^+, X_2^-, X_3^+, X_3^-$ denote the faces of the cube with outward normals directed in a positive or negative direction of the corresponding coordinate axes, a was the side length of the reference volume cube, $\varepsilon^{(0)}$ was the value of applied strain, u_1, u_2, u_3 were the displacements in x_1, x_2, x_3 directions correspondingly;

(c) The FEA simulations were performed and the output file was imported into Matlab r2009b (www.mathworks.com);

(d) Stress volume averages $\left\langle \sigma_{ij}^{(k)} \right\rangle_{RVE}$ (k is the loadcase number) were calculated;

(e) Stiffness contribution tensor N_{ijkl} was calculated: e.g. from the first loadcase (uniaxial tension in x_1 direction):

$$N_{ij11} = \frac{\sigma_{ij}^{(0)} - \left\langle \sigma_{ij}^{(1)} \right\rangle_{RVE}}{\varepsilon^{(0)}} \tag{4.1}$$

where $\sigma_{ij}^{(0)}$ are the stresses in the matrix material subjected to $\varepsilon_{11} = \varepsilon^{(0)}$, $\left\langle \sigma_{ij}^{(1)} \right\rangle_{RVE}$ are the stress volume average in the porous material subjected to $\varepsilon_{11} = \varepsilon^{(0)}$. The remaining components can be determined from the symmetry conditions. Both stiffness and compliance contribution tensors are symmetric with respect to $i \leftrightarrow j$, $k \leftrightarrow l$, $(ij) \leftrightarrow (kl)$;

(f) compliance contribution tensor H_{ijkl} was then expressed in terms of N_{ijkl}:

$$H_{ijkl} = -S_{ijmn}^{(0)} N_{mnpq} S_{pqkl}^{(0)} \tag{4.2}$$

where $S_{ijkl}^{(0)}$ are the components of the compliance tensor of the matrix material.

In the above procedure, the size of the reference volume was chosen to simulate remote loading and to eliminate boundary effects. We performed the sensitivity studies for different reference volume sizes (similar to the approach used in Tsukrov and Novak (2002), Teng (2010)) and determined that the reference volume with sides five times greater than the largest dimensions of the pore satisfies such requirements.

5. Pores in isotropic PyC matrix

5.1. Contribution of pores to effective elastic properties

The algorithm presented in Section 4.2 was used to evaluate the contributions of actual pores to the overall elastic properties of porous pyrolytic carbon. In this section we consider pores in the isotropic PyC with the properties derived using the method described in Section 2 as $E_0 = 12.79$ GPa, $\nu_0 = 0.39$.

As an illustration, all components of the H-tensor for a pore shape shown in Fig. 4 can be found and presented in the matrix form (Voigt convention, see Kachanov et al., 2003 as follows:

$$\begin{bmatrix} \overline{H}_{1111} & \overline{H}_{1122} & \overline{H}_{1133} & 2\overline{H}_{1112} & 2\overline{H}_{1123} & 2\overline{H}_{1131} \\ \overline{H}_{2211} & \overline{H}_{2222} & \overline{H}_{2233} & 2\overline{H}_{2212} & 2\overline{H}_{2223} & 2\overline{H}_{2231} \\ \overline{H}_{3311} & \overline{H}_{3322} & \overline{H}_{3333} & 2\overline{H}_{3312} & 2\overline{H}_{3323} & 2\overline{H}_{3331} \\ 2\overline{H}_{1211} & 2\overline{H}_{1222} & 2\overline{H}_{1233} & 4\overline{H}_{1212} & 4\overline{H}_{1223} & 4\overline{H}_{1231} \\ 2\overline{H}_{2311} & 2\overline{H}_{2322} & 2\overline{H}_{2333} & 4\overline{H}_{2312} & 4\overline{H}_{2323} & 4\overline{H}_{2331} \\ 2\overline{H}_{3111} & 2\overline{H}_{3122} & 2\overline{H}_{3133} & 4\overline{H}_{3112} & 4\overline{H}_{3123} & 4\overline{H}_{3131} \end{bmatrix}$$
$$= \begin{bmatrix} 1.7527 & -0.5080 & -0.5088 & 0.0110 & -0.2838 & -0.2329 \\ -0.5080 & 2.3586 & -0.5658 & 0.1435 & -0.0953 & 0.0511 \\ -0.5088 & -0.5658 & 2.5908 & 0.0488 & 0.7214 & 0.3879 \\ 0.0110 & 0.1435 & 0.0488 & 5.2280 & 0.1409 & 0.2653 \\ -0.2838 & -0.0953 & 0.7214 & 0.1409 & 6.1285 & -0.0245 \\ -0.2329 & 0.0511 & 0.3879 & 0.2653 & -0.0245 & 5.6228 \end{bmatrix} \tag{5.1}$$

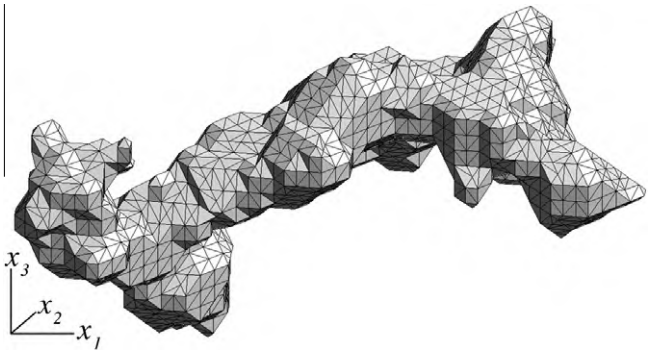

Fig. 4. Finite element mesh of an irregular pore.

where the dimensionless components of H are defined as $\overline{H}_{ijkl} = \frac{VE_0}{V_P} H_{ijkl}$ (recall that V_P/V is the volume fraction of the pore in the reference volume). The resulting matrix should be symmetric from mechanical considerations. Numerical values of the corresponding off-diagonal terms obtained by processing FEA data were within 2% of each other; symmetrization was performed by taking the average of the two numbers.

As presented in Section 3, the overall compliance of porous material is given by $\mathbf{S} = \mathbf{S}_0 + H_{RVE}$, where $\mathbf{S}_0$ is the compliance tensor of the PyC. Tensor H_{RVE} for the representative volume element can be found in terms of the H-tensors of individual pores. In particular, at low porosities, the non-interaction approximation (dilute limit) can be used so that $H_{RVE} = \sum_i H^{(i)}$ where summation is performed over all pores present in the RVE.

In the case of *parallel pores* of the same shape, the non-interaction approximation yields

$$H_{RVE} = \frac{p}{E_{(0)}} \overline{H} \tag{5.2}$$

where $\overline{H}$ is the dimensionless compliance contribution tensor of the considered pore type and p is the porosity (volume fraction of pores) defined as $p = \sum_i V_P^{(i)} / V^{RVE}$.

Thus, all effective elastic parameters of porous material can be found. The effective Young's moduli, for example, are given by

$$\frac{E_i}{E_0} = \frac{1}{1 + p\widetilde{E}_i} \tag{5.3}$$

where E_i is the Young's modulus in the x_i-direction and $\widetilde{E}_i$ is equal to $\overline{H}_{iiii}$ (no summation over repeating indices).

In the case of non-parallel orientation of pores, summation can be substituted by integration over the orientation angles multiplied by the corresponding orientation distribution density. For random orientational distribution of pores of the same type characterized by tensor H, this procedure results in an isotropic H_{RVE}-tensor characterized by two invariants:

$$\widetilde{H}_K = \frac{H_{iijj}}{3}, \quad \widetilde{H}_G = \frac{3H_{ijij} - H_{iijj}}{15} \tag{5.4}$$

It can be shown that these invariants are related to the changes in the overall bulk and shear moduli of the material containing *randomly oriented pores* of the same shape (see Wu, 1966 and David and Zimmerman, 2011). Utilizing Wu's strain concentration tensor $\mathbf{T}$, related to H and $\mathbf{S}_0$ as $H = \mathbf{T}:\mathbf{S}_0$ (David and Zimmerman, 2011), we obtain the following expression for the overall bulk and shear moduli:

$$\frac{K}{K_0} = \frac{1}{1 + p\widetilde{K}}, \quad \frac{G}{G_0} = \frac{1}{1 + p\widetilde{G}} \tag{5.5}$$

where $K_0 = \frac{E_0}{3(1-2\nu_0)}$ and $G_0 = \frac{G_0}{2(1+\nu_0)}$ are the bulk and shear moduli of the matrix material. The pore contributions $\widetilde{K}$ and $\widetilde{G}$ are found as in Wu (1966).

$$\widetilde{K} = \frac{T_{iijj}}{3}, \quad \widetilde{G} = \frac{3T_{ijij} - T_{iijj}}{15} \tag{5.6}$$

These parameters are sometimes called the pore compressibility and pore shear compliance.

Note that, as porosity increases, the non-interaction approximation becomes inaccurate and more advanced first order micromechanical schemes are usually used, for example, Mori–Tanaka (Mori and Tanaka, 1973; Benveniste, 1987) or differential (Salganik, 1973; McLaughlin, 1977; Zimmerman, 1986, 1991a). The predictions of these schemes can be obtained in terms of the non-interaction compliance contribution tensors (Eroshkin and Tsukrov, 2005).

Table 1 presents values of $\widetilde{E}_i$ (contribution to effective Young's moduli by parallel pores of the same shape), $\widetilde{K}$ and $\widetilde{G}$ (contributions to the bulk and shear moduli of the effective isotropic material in the case of randomly oriented pores) for several selected pores of irregular shapes observed in PyC. All of these pores are shown in a fixed coordinate system aligned with the edges of the cubic specimen described in Section 4.2. Relative deviations from the average values of the parameters $\widetilde{E}_1$, $\widetilde{E}_2$, $\widetilde{E}_3$, $\widetilde{K}$, $\widetilde{G}$ are denoted as $\delta\widetilde{E}_i$, $\delta\widetilde{K}$, $\delta\widetilde{G}$, e. g. $\delta\widetilde{E}_1 = 100\% \cdot \left(\widetilde{E}_1 - \widetilde{E}_1^{avg}\right)/\widetilde{E}_1^{avg}$. In the end of the table, the corresponding values for spheroidal cavities (sphere, prolate spheroid with axes' ratio 1:1:5 and oblate spheroid 1:1:0.2) are shown for comparison. It is obvious that values of $\widetilde{E}_1, \widetilde{E}_2, \widetilde{E}_3$ depend on the choice of the global coordinate system, while $\widetilde{K}$ and $\widetilde{G}$ are invariant.

One immediate observation is that parameters characterizing contributions of the irregularly shaped pores in PyC are very close to each other, particularly pore compressibility $\widetilde{K}$ and shear compliance $\widetilde{G}$. Most values of $\widetilde{K}$ and all analyzed values of $\widetilde{G}$ are within 5% of their average values. At the same time, difference between these average values and the corresponding parameters for the considered spheroids is much greater: 21.2%, 12.5% and 58.6% for $\widetilde{K}$, and 9.2%, 8.1% and 26.4% for $\widetilde{G}$. As previously mentioned in the literature (see, for example Zimmerman, 1991b) the spherical cavity is the stiffest possible pore shape ($\widetilde{K}$=4.253) while oblate spheroids (and, in the limiting case, penny-shaped cracks) are the most compliant objects.

We speculate that the observed closeness of the overall compliance contribution parameters of the considered PyC pores is caused by the chemical vapor infiltration used for the material manufacture. The pore surface-to-volume ratio, which is one of the characteristic parameters of infiltration, can also be an essential parameter for compressibility and shear compliance of pores with similar aspect ratios (not crack-like). In the 2D case, this fact was previously observed by Zimmerman (1991b) and Tsukrov and Novak (2002).

5.2. Approximation of irregularly shaped pores by ellipsoids using principal components analysis

It is common practice in evaluating contribution to effective properties by three-dimensional pores (and other defects) to assume that the pores have ellipsoidal shapes. The main reason is that only such shapes possess the property of uniform eigenstrain under remotely applied loading, so that the analytical solutions for strains and stresses around them can be utilized (Eshelby, 1957, 1959; Mura, 1987).

In the case of highly irregular defect shapes, one possible approach is to find the bounds of individual pore contributions by considering the inscribed and circumscribed ellipsoids constructed for such a pore (Hill, 1963; Huet et al., 1991). However, for the shapes considered in Table 1 of the previous section, such an approach would result in extremely wide bounds due to large differences between the dimensions of the inscribed and circumscribed ellipsoids.

When pores are approximated by ellipsoids, two major issues have to be addressed: (1) the choice of the best approximation of real pore shape by an ellipsoid (orientations and lengths of principal axes) and (2) accuracy of the chosen approximation. An approach utilizing 2D micrographs to select the approximating spheroids is discussed in Laraia et al. (1994), Prokopiev and Sevostianov (2006). In this section of the paper, we propose a principal component analysis (PCA) approach (Jolliffe, 2002) utilizing the experimentally obtained 3D μCT data to construct the approximating ellipsoids, and evaluate the accuracy of the approach in terms of effective property predictions.

In the presentation of PCA approach, the notation x, y, z for the point coordinates will be used. Processing the μCT data,

Table 1
Contributions of selected pores to effective elastic properties.

Pore shape	$\widetilde{E}_1$	$\delta\widetilde{E}_1$ (%)	$\widetilde{E}_2$	$\delta\widetilde{E}_2$ (%)	$\widetilde{E}_3$	$\delta\widetilde{E}_3$ (%)	$\widetilde{K}$	$\delta\widetilde{K}$ (%)	$\widetilde{G}$	$\delta\widetilde{G}$ (%)
	1.753	−2.7	2.359	−8.5	2.591	14.1	5.507	2.0	2.012	1.0
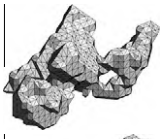	1.711	−5.0	2.674	3.7	2.176	−4.2	5.327	−1.3	1.964	−1.3
	1.831	1.7	2.348	−8.9	2.499	10.0	5.402	0.1	1.999	0.4
	1.931	7.2	2.871	11.4	1.896	−16.5	5.354	−0.8	1.992	0.1
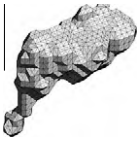	1.491	−17.2	2.765	7.3	2.112	−6.8	5.117	−5.2	1.932	−3.0
	2.070	14.9	2.661	3.2	2.154	−5.2	5.605	3.8	2.056	3.2
	1.994	10.7	2.377	−7.8	2.112	−7.0	5.276	−2.3	1.951	−2.0
	1.630	−9.5	2.568	−0.4	2.626	15.6	5.609	3.9	2.024	1.7
Arith. mean	**1.801**		**2.578**		**2.271**		**5.399**		**1.991**	
Std. deviation	**0.194**		**0.199**		**0.265**		**0.169**		**0.041**	
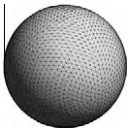	1.905	5.8	1.904	−26.1	1.905	−16.1	4.253	−21.2	1.808	−9.2
	2.379	32.1	2.381	−7.6	1.121	−50.6	4.725	−12.5	1.830	−8.1
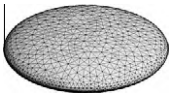	1.266	−29.7	1.266	−50.1	5.918	160.6	8.561	58.6	2.517	26.4

the pores in the image were labeled and the surface of the pores was extracted to obtain input points (x_i, y_i, z_i) for the estimation of geometrical properties using PCA. Additionally, the volume and center of mass of each pore were determined for further use in the fitting process. A statistical method for describing variations or similarities in data is given by the variance or covariance of a data set (Jolliffe, 2002). In our case, the data set is comprised of all the surface points of the pore, which are a reduced representation of the complete body of the pore structure. It is possible to simplify the description of a pore in the composite to be represented by only a few characteristic parameters by applying the PCA methods to the data set. Therefore, it is necessary to compute the variance in 3D points and assemble the covariance matrix of the pore with all the necessary information to describe a simplified representation of the pore geometry. The covariance of two sets of variables, for example (X, Y), is defined as:

$$\mathrm{cov}(X,Y) = \frac{\sum_{i=1}^{n}(x_i - \bar{x})(y_i - \bar{y})}{n-1} \tag{5.7}$$

For the direct estimation of the geometrical parameters of the pore in a local coordinate system, it is advantageous to subtract the center of mass $(\overline{X},\overline{Y},\overline{Z})$ from each point in the point set before the covariance matrix is constructed. This sets the origin of the coordinate system to the center of mass and relates all geometrical parameters to the local coordinate system.

Using the definition of the covariance of the three dimension in space for the point set the covariance matrix is:

$$\mathbf{C}=\begin{bmatrix}\mathrm{cov}(X,X) & \mathrm{cov}(X,Y) & \mathrm{cov}(X,Z)\\ \mathrm{cov}(Y,X) & \mathrm{cov}(Y,Y) & \mathrm{cov}(Y,Z)\\ \mathrm{cov}(Z,X) & \mathrm{cov}(Z,Y) & \mathrm{cov}(Z,Z)\end{bmatrix} \tag{5.8}$$

This matrix is symmetric and, using the spectral theorem of linear algebra, we apply the eigenvector decomposition to rewrite the covariance matrix in the form suggested by Bronstein and Semendjajew (2006)

$$\mathbf{C}=\mathbf{Q}\ \mathbf{\Lambda}\ \mathbf{Q}^{\mathbf{T}} \tag{5.9}$$

Matrix $\mathbf{\Lambda}=diag(\lambda_1,\lambda_2,\lambda_3)$ is the diagonal matrix of eigenvalues

$$\mathbf{\Lambda}=\begin{bmatrix}\lambda_1 & 0 & 0\\ 0 & \lambda_2 & 0\\ 0 & 0 & \lambda_3\end{bmatrix}, \tag{5.10}$$

where $\sqrt{\lambda_1},\sqrt{\lambda_2}$ and $\sqrt{\lambda_1}$ are the semi-axes of the approximating ellipsoid and $\mathbf{Q}$ is the matrix of eigenvectors composed of the direction cosines of the ellipsoid's principal axes organized in columns. Thus, all parameters of the approximating ellipsoid are defined. The resulting surface has the same variance as the original set of surface data points.

For the pore considered in Section 5.1 (Fig. 4), the above procedure results in the approximating ellipsoid with semi-axes $a=0.246d$, $b=0.308d$, $c=0.862d$, where d is the length of the pore in x direction, see Fig. 5. The Euler angles defining orientation of the ellipsoid ($ZY'Z''$ convention) are $-24.2°$, $77.9°$ and $-130.0°$, correspondingly. The $\overline{H}$-tensor of the ellipsoid is

$$\begin{bmatrix}\overline{H}_{1111} & \overline{H}_{1122} & \overline{H}_{1133} & 2\overline{H}_{1112} & 2\overline{H}_{1123} & 2\overline{H}_{1131}\\ \overline{H}_{2211} & \overline{H}_{2222} & \overline{H}_{2233} & 2\overline{H}_{2212} & 2\overline{H}_{2223} & 2\overline{H}_{2231}\\ \overline{H}_{3311} & \overline{H}_{3322} & \overline{H}_{3333} & 2\overline{H}_{3312} & 2\overline{H}_{3323} & 2\overline{H}_{3331}\\ 2\overline{H}_{1211} & 2\overline{H}_{1222} & 2\overline{H}_{1233} & 4\overline{H}_{1212} & 4\overline{H}_{1223} & 4\overline{H}_{1231}\\ 2\overline{H}_{2311} & 2\overline{H}_{2322} & 2\overline{H}_{2333} & 4\overline{H}_{2312} & 4\overline{H}_{2323} & 4\overline{H}_{2331}\\ 2\overline{H}_{3111} & 2\overline{H}_{3122} & 2\overline{H}_{3133} & 4\overline{H}_{3112} & 4\overline{H}_{3123} & 4\overline{H}_{3131}\end{bmatrix}$$

$$=\begin{bmatrix}2.0273 & -0.5324 & -0.5780 & 0.4421 & 0.0244 & -0.3952\\ -0.5324 & 1.7434 & -0.5355 & 0.5035 & 0.0759 & 0.0210\\ -0.5780 & -0.5355 & 2.6852 & -0.1349 & 0.0193 & -0.3206\\ 0.4421 & 0.5035 & -0.1349 & 4.5872 & -0.5115 & 0.1817\\ 0.0244 & 0.0759 & 0.0193 & -0.5115 & 5.6470 & 0.4647\\ -0.3952 & 0.0210 & -0.3206 & 0.1817 & 0.4647 & 5.8818\end{bmatrix} \tag{5.11}$$

Comparing its components with the values for the original pore (5.1), we observe that diagonal terms are relatively close. No conclusive observation for the off-diagonal terms can be made. Introducing the Euclidean norm of the 4th rank tensor $\|\mathbf{S}\|=\sqrt{S_{ijkl}S_{ijkl}}$ (summation over the repeating indices), the relative distance between the compliance contribution tensor of the actual pore and its approximation is

$$\Delta=\frac{\|\mathbf{S}^{exact}-\mathbf{S}^{appr}\|}{\|\mathbf{S}^{exact}\|}=\frac{\sqrt{\left(S^{exact}_{ijkl}-S^{appr}_{ijkl}\right)\left(S^{exact}_{ijkl}-S^{appr}_{ijkl}\right)}}{\left(S^{exact}_{pqrs}S^{exact}_{pqrs}\right)}=0.2431 \tag{5.12}$$

Note that this parameter is called error in Sevostianov and Kachanov (2008), who utilized it to analyze elastic symmetries.

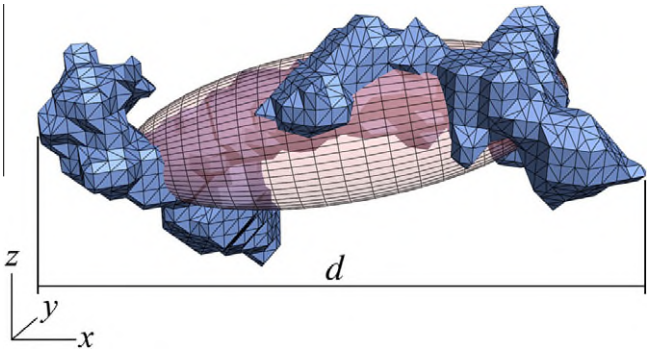

Fig. 5. Pore and approximating ellipsoid.

To provide more mechanically meaningful comparison, Table 2 presents compressibility and shear compliance values for approximating ellipsoids compared to the corresponding parameters of the original shapes of the selected pores. The contribution of ellipsoids (H-tensor) was found by utilizing the analytical solutions of Eshelby (1957), Eshelby (1959).

Analyzing the relative error, defined as $\delta\widetilde{K}=100\%\cdot(\widetilde{K}_P-\widetilde{K}_{ELL})/\widetilde{K}_P$, $\delta\widetilde{G}=100\%\cdot\left(\widetilde{G}_P-\widetilde{G}_{ELL}\right)/\widetilde{G}_P$, we conclude that for most shapes the PCA approximation of actual pores by ellipsoids produces discrepancy on the order of 10–20%. Also, there is no pronounced tendency of the approximation to over- or underestimate the change in stiffness of the porous C/C material.

6. Pores in unidirectional C/C composite

In this section, we investigate contributions of the pores to the effective elastic properties of unidirectional C/C composite. Fig. 6 shows the entire unidirectional region of μCT-scanned sample with the complete set of pores (porosity $p_0=9.13\%$, see Fig. 6). This set includes all pores with the smallest dimension greater than 50 μm (43 pores total). Smaller pores were excluded from consideration because their contribution to the overall response was minimal. Note that crack-like pores, even of negligible volume fraction, can contribute significantly to the reduction of the overall stiffness; however, no such pores were observed in the region.

Each of the pores was processed separately to determine its compliance contribution tensor. The example of a pore observed in a unidirectional C/C composite is shown in Fig. 7. Fibers of the specimen have a diameter of 10 μm; the remaining space is filled with layers of PyC deposited on fibers.

In the modeling procedure, pores were assumed to be placed in a homogenized transversely isotropic material consisting of unidirectional carbon fibers and PyC matrix. It was assumed that a typical fiber is surrounded by two cylindrically orthotropic concentric layers of PyC having different levels of texture. Each level is characterized by Fisher parameter κ (see Section 2), as schematically shown in Fig. 8. This microstructure is described as Mat_B in Piat et al. (2008). Table 3 provides typical dimensions, levels of texture, and material properties of carbon fiber/PyC (FPC) mixture. The properties of the T300 carbon fiber are taken from Wagoner and Bacon (1989). Note that fiber volume fraction in this mixture is $V_f=0.189$.

The effective properties of FPC were found utilizing recently obtained elasticity solutions (Tsukrov and Drach, 2010) in combination with the composite cylinder assemblage approach (Hashin and Rosen, 1964; Hashin, 1990) and effective medium method (Kröner, 1958; Hill, 1965; Budiansky, 1965). The outline of the micromechanical procedure can be found in Tsukrov et al. (2009)

Table 2
Irregular pore shapes approximated by ellipsoids. $\widetilde{K}_{ELL}$ and $\widetilde{G}_{ELL}$ are the compressibility and shear compliance values of ellipsoids; these parameters for pores, $\widetilde{K}_P$ and $\widetilde{G}_P$ are copied from Table 1 for comparison.

Pore	$\widetilde{K}_P$	$\widetilde{K}_{ELL}$	$\delta\widetilde{K}$ (%)	$\widetilde{G}_P$	$\widetilde{G}_{ELL}$	$\delta\widetilde{G}$ (%)
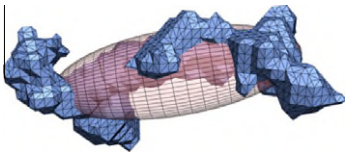	5.507	4.927	10.5	2.012	1.933	3.9
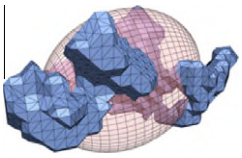	5.327	6.668	−25.4	1.964	2.226	13.3
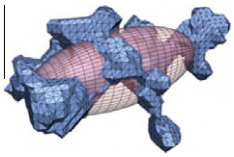	5.402	4.840	10.4	1.999	1.914	4.3
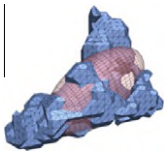	5.354	4.782	10.7	1.992	1.901	4.6
	5.117	4.970	2.9	1.932	1.934	−0.1

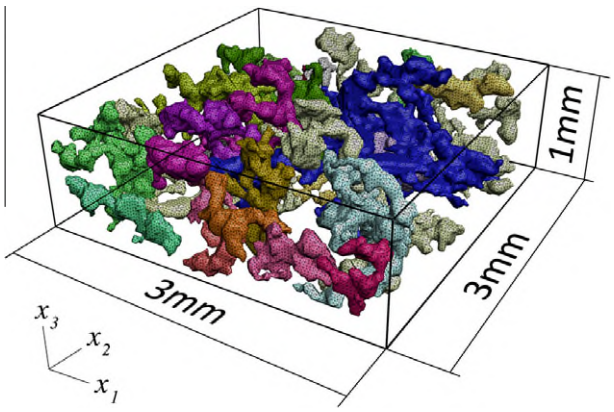

Fig. 6. Pore setup in a piece of unidirectional layer in C/C composite.

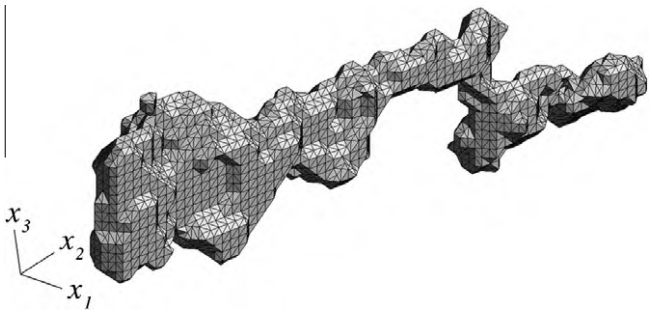

Fig. 7. Elongated pore in unidirectional C/C composite.

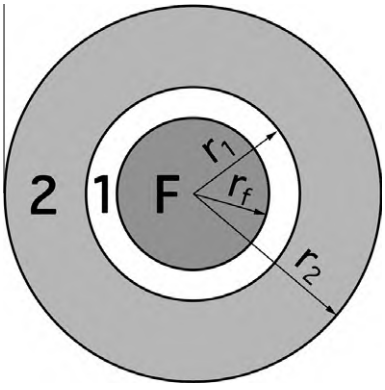

Fig. 8. Carbon fiber surrounded by two layers of PyC.

its application to the considered material system results in the following prediction for the effective elastic properties of FPC:

$$
\begin{aligned}
E_1^{FPC} &= 59.44\ \text{GPa} \\
E_2^{FPC} &= E_3^{FPC} = 10.94\ \text{GPa} \\
\nu_{23}^{FPC} &= 0.3973 \\
\nu_{12}^{FPC} &= \nu_{13}^{FPC} = 0.3229 \\
G_{12}^{FPC} &= G_{31}^{FPC} = 4.62\ \text{GPa}
\end{aligned}
\tag{6.1}
$$

The compliance contribution tensor of the pore shown in Fig. 7 placed in the homogeneous transversely isotropic material with

Table 3
Material properties of C/C composite constituents.

	r (μm)	κ	C_{rr} (GPa)	$C_{\theta\theta}$ (GPa)	C_{zz} (GPa)	$C_{r\theta}$ (GPa)	$C_{\theta z}$ (GPa)	C_{rz} (GPa)	$G_{r\theta}$ (GPa)	$G_{\theta z}$ (GPa)	G_{rz} (GPa)
Fiber	5	–	19.13	19.13	207.82	9.13	7.35	7.35	5.00	22.20	22.20
Layer 1	6.5	0.1	25.02	25.01	25.01	15.48	15.51	15.48	4.78	4.75	4.78
Layer 2	11.5	100	18.12	38.80	38.80	13.15	19.47	13.15	1.94	9.66	1.94

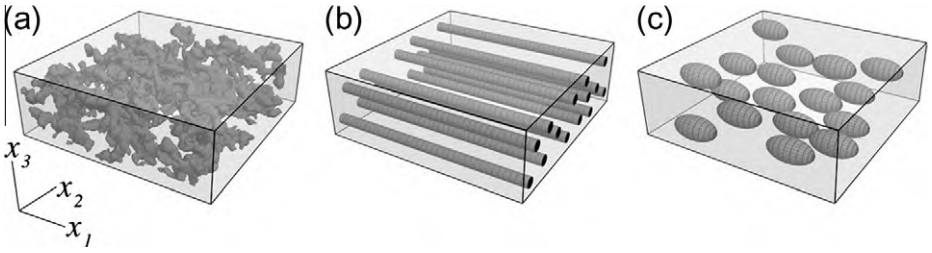

Fig. 9. Schematic representation of: (a) real pore setup in UD layer of C/C composite; (b) approximation of pores by cylinders; and (c) approximation of pores by prolate spheroids with aspect ratio 2:1.

properties given in (6.1) is calculated using procedure presented in 4.2 as

$$\begin{bmatrix} \overline{H}_{1111} & \overline{H}_{1122} & \overline{H}_{1133} & 2\overline{H}_{1112} & 2\overline{H}_{1123} & 2\overline{H}_{1131} \\ \overline{H}_{2211} & \overline{H}_{2222} & \overline{H}_{2233} & 2\overline{H}_{2212} & 2\overline{H}_{2223} & 2\overline{H}_{2231} \\ \overline{H}_{3311} & \overline{H}_{3322} & \overline{H}_{3333} & 2\overline{H}_{3312} & 2\overline{H}_{3323} & 2\overline{H}_{3331} \\ 2\overline{H}_{1211} & 2\overline{H}_{1222} & 2\overline{H}_{1233} & 4\overline{H}_{1212} & 4\overline{H}_{1223} & 4\overline{H}_{1231} \\ 2\overline{H}_{2311} & 2\overline{H}_{2322} & 2\overline{H}_{2333} & 4\overline{H}_{2312} & 4\overline{H}_{2323} & 4\overline{H}_{2331} \\ 2\overline{H}_{3111} & 2\overline{H}_{3122} & 2\overline{H}_{3133} & 4\overline{H}_{3112} & 4\overline{H}_{3123} & 4\overline{H}_{3131} \end{bmatrix}$$

$$= \begin{bmatrix} 7.1399 & -2.5336 & -1.7562 & -2.4690 & 0.6108 & -0.0284 \\ -2.5336 & 82.7547 & -14.3999 & -1.7062 & -0.5625 & -0.4366 \\ -1.7562 & -14.3999 & 40.9100 & -0.2002 & -7.1548 & 0.9899 \\ -2.4690 & -1.7062 & -0.2002 & 110.5299 & 0.2619 & -1.8915 \\ 0.6108 & -0.5625 & -7.1548 & 0.2619 & 156.5124 & -1.8914 \\ -0.0284 & -0.4366 & 0.9899 & -1.8915 & -1.8914 & 74.3881 \end{bmatrix} \tag{6.2}$$

where components of $\overline{H}$ are normalized with respect to the modulus E_1^{FPC} and volume fraction of the pore V_p in the reference volume V : $\overline{H}_{ijkl} = \frac{E_1^{FPC} V_p}{V} H_{ijkl}$.

After calculating the cavity compliance tensors for all pores shown in Fig. 6, we can assume the non-interaction approximation for the total porosity of less than 10%. Utilizing formulae (3.2) and (3.3), and extracting the engineering constants from the effective material compliance matrix, the following anisotropic material parameters are obtained:

$$\begin{aligned} &E_1 = 47.62\ \text{GPa}, \quad E_2 = 8.72\ \text{GPa}, \quad E_3 = 9.12\ \text{GPa}, \\ &\nu_{12} = 0.3191, \quad \nu_{23} = 0.3610, \quad \nu_{13} = 0.3048, \\ &G_{12} = 3.96\ \text{GPa}, \quad G_{23} = 3.24\ \text{GPa}, \quad G_{31} = 4.00\ \text{GPa} \end{aligned} \tag{6.3}$$

Note that the anisotropy of the effective material is of a general type; however, the deviation from transverse isotropy is not significant. The appropriate symmetrization produces transversely isotropic material with

$$\begin{aligned} &E_1 = 47.62\ \text{GPa}, \quad E_2 = E_3 = 8.92\ \text{GPa}, \\ &\nu_{12} = \nu_{13} = 0.3120, \quad \nu_{23} = 0.3610 \\ &G_{12} = G_{13} = 3.98\ \text{GPa} \end{aligned} \tag{6.4}$$

The error of such approximation, expressed in terms of the Euclidean norm (as defined by Eq. 5.12), is $\Delta = 0.0054$. Thus, the presence of irregularly shaped pores does not introduce a significant deviation from the transversely isotropic behavior of unidirectional C/C composites.

In micromechanical modeling of unidirectional composites pores are often assumed to be aligned with fibers and propagate continuously with constant cross-section (see Fig. 9b). With these assumptions, the rule of mixtures can be used to predict longitudinal properties of the composite and plane strain solutions can be utilized for transverse response. For the considered material system we obtain: $E_1 = 54.01$ GPa and $E_2 = 8.59$ GPa. As can be seen, the rule of mixtures significantly overestimates the longitudinal and slightly underestimates the transverse stiffness of the material by assuming the arrangement of material that provides maximum resistance to unidirectional loading. For comparison, parallel 2:1 spheroidal pores randomly distributed in the same transversely isotropic matrix (non-interaction approximation, see Fig. 9c) result in the effective moduli: $E_1 = 50.40$ GPa and $E_2 = 9.03$ GPa.

Thus, even though the rule of mixtures provides a reasonably good estimate for longitudinal modulus of porous UD C/C composites, the approximation of pores by 2:1 aligned spheroidal shapes (this aspect ratio seems to be close to the average eccentricity of the pores) produces better overall predictions of the effective Young's moduli.

7. Conclusions

CVI infiltrated C/C composites contain 3D pores of irregular shapes that can be extracted by X-ray computed microtomography. The procedure proposed in this paper to evaluate their contributions to the effective elastic properties is based on the compliance contribution tensors of individual pores calculated by FEA. The obtained tensors can then be used in a number of micromechanical schemes; explicit expressions for non-interaction approximation and Mori–Tanaka scheme are given in Section 3. The PyC matrix material is modeled assuming a von-Mises-Fisher distribution of highly textured transversely isotropic domains of submicron size.

It was observed that the parameters characterizing contributions of individual pores to effective elastic moduli (especially, contributions to the bulk and shear moduli of the effective isotropic material in the case of randomly oriented pores of the same shape) were very similar. We speculate that this closeness in values is caused by the chemical vapor infiltration process used for the material manufacture.

The principal component analysis approach to approximating the real pore geometry by ellipsoidal shapes was presented in Section 5.2. It was observed that for most shapes, the PCA

approximation produces discrepancy on the order of 10–20% in the pore compressibility and shear compliance. This approach may be useful when bounding of the effective properties by analyzing inscribed and circumscribed ellipsoids is not practical due to large difference in the ellipsoids' dimensions.

Contribution of all pores present in a $3 \times 3 \times 1$ mm region of unidirectional C/C composite was analyzed in Section 6. With porosity of 9.13% the reductions of Young's moduli E_1, E_2, E_3 were 19.9%, 20.3% and 16.6% correspondingly. It was determined that irregularity of elongated pore shapes does not introduce a significant deviation from the transversely isotropic behavior of unidirectional C/C composites. Also, comparing the approximations of pores by long cylinders and 2:1 spheroidal shapes (assuming the same porosity), we conclude that approximation by spheroids produces better overall predictions of the effective Young's moduli.

Acknowledgements

The authors gratefully acknowledge the financial support of the National Science Foundation (NSF) and German Science Foundation (DFG) through the Grant DMR-0806906 "Materials World Network: Multi- Scale Study of Chemical Vapor Infiltrated Carbon/Carbon Composites". Romana Piat also acknowledges the support of DFG through the project PI 785/1-1. The authors would like to thank Robert Zimmerman for his insightful comments on compressibility and shear compliance of pores. Galyna Stasiuk (KIT) participated in determining the parameters for approximations of pores by ellipsoids. Sam Wesley (UNH) participated in the μCT data processing as a part of his undergraduate student research program.

References

Arns, Ch.H., Knackstedt, M., Pinczewski, W., Garboczi, E., 2002. Computation of linear elastic properties from micrographic images: methodology and agreement between theory and experiment. Geophysics 67, 1396–1405.

Benveniste, Y., 1987. A new approach to the application of Mori–Tanaka theory in composite materials. Mech. Mater. 6, 147–157.

Bortchagovsky, E.G., Reznik, B., Gerthsen, D., Pfrang, A., Schimmel, T., 2003. Optical properties of pyrolytic carbon deposits deduced from measurements of the extinction angle by polarized light microscopy. Carbon 41, 2430–2433.

Böhlke, T., Jöchen, K., Piat, R., Langhoff, T.-A., Tsukrov, I., Reznik, B., 2010. Elastic properties of pyrolytic carbon with axisymmetric textures. Tech. Mech. 30 (4), 343–353 <http://www.uni-magdeburg.de/ifme/zeitschrift_tm/2010_Heft4/04_Boehlke.pdf>.

Böhm, H.J., Han, W., Eckschlager, A., 2004. Multi-inclusion unit cell studies of reinforcement stresses and particle failure in discontinuously reinforced ductile matrix composites. Comput. Model. Eng. Sci. 5, 5–20.

Bronstein, I.N., Semendjajew, K.A., 2006. Taschenbuch der Mathematik. Auflage, BG Teubner Verlagsgesellschaft, Stuttgart Leipzig und Verlag Nauka, Moskau.

Budiansky, B., 1965. On the elastic moduli of some heterogeneous materials. J. Mech. Phys. Solids 13, 223–227.

David, E., Zimmerman, R.W., 2011. Compressibility and shear compliance of spheroidal pores: exact derivation via the Eshelby tensor, and asymptotic expressions in limiting cases. Int. J. Solids Struct. 48, 680–686.

Ekneligoda, T.C., Zimmerman, R.W., 2006. Compressibility of two-dimensional pores having n-fold axes of symmetry. Proc. Roy. Soc. Lond. Ser. A 462, 1933–1947.

Ekneligoda, T.C., Zimmerman, R.W., 2007. Estimating the elastic moduli of sandstones using two-dimensional pore space images. In: Proceedings of 1st Sri-Lanka Geotech. Soc. International Conference Soil & Rock Eng., Colombo, Sri Lanka.

Ekneligoda, T.C., Zimmerman, R.W., 2008. Shear compliance of two-dimensional pores possessing N-fold axis of rotational symmetry. Proc. Roy. Soc. Lond. Ser. A 464, 759–775.

Eroshkin, O., Tsukrov, I., 2005. On micromechanical modeling of particulate composites with inclusions of various shapes. Int. J. Solids Struct. 42, 409–427.

Eshelby, J.D., 1957. The determination of the elastic field of an ellipsoidal inclusion and related problems. Proc. Roy. Soc. Lond. Ser. A 241, 376–396.

Eshelby, J.D., 1959. The elastic field outside an ellipsoidal inclusion. Proc. Roy. Soc. Lond. Ser. A 252, 561–569.

Faivre, G., 1964. Déformations de cohérence d'un précipité quadratique. Phys. Status Solidi 35, 249–259.

Fokin, A.G., 1972. Solution of statistical problems in elasticity theory in the singular approximation. J. Appl. Mech. Tech. Phys. 13, 85–89.

Fokin, A.G., 1973. Singular approximation for the calculation of the elastic properties of reinforced systems. Mech. Compos. Mater. 9, 445–449.

Gebert, J.-M., Wanner, A., Piat, R., Guichard, M., Rieck, S., Paluszynski, B., Böhlke, T., 2008. Application of the micro-computed tomography for analyses of the mechanical behavior of brittle porous materials. Mech. Adv. Mater. Struct. 15, 467–473.

Gebert, J.-M., Reznik, B., Piat, R., Viering, B., Weidenmann, K., Wanner, A., Deutschmann, O., 2010. Elastic constants of high-texture pyrolytic carbon measured by ultrasound phase spectroscopy. Carbon 48 (12), 3647–3650.

González, C., Segurado, J., LLorca, J., 2004. Numerical simulation of elasto-plastic deformation of composites: evolution of stress microfields and implications for homogenization models. J. Mech. Phys. Solids 52, 1573–1593.

Gray, R.J., Cathcart, J.V., 1966. Polarized light microscopy of pyrolytic carbon deposits. J. Nucl. Mater. 19, 81–89.

Hashin, Z., Rosen, B.W., 1964. The elastic moduli of fiber reinforced materials. J. Appl. Mech. 31, 223.

Hashin, Z., 1990. Thermoelastic properties and conductivity of carbon/carbon fiber composites. Mech. Mater. 8, 293–308.

Hill, R., 1963. Elastic properties of reinforced solids: some theoretical principles. J. Mech. Phys. Solids 11, 357–372.

Hill, R., 1965. A self-consistent mechanics of composite materials. J. Mech. Phys. Solids 13, 213–222.

Huet, C., Navi, P., Roelfstra, P., 1991. A homogenization technique based on Hill's modification theorem. In: Maugin, G. (Ed.), Continuum Models and Discrete Systems. Longman, Harlow, UK, pp. 135–143.

Ibanez, L., Schroeder, W., Ng, L., Cates, J., 2005. The ITK Software Guide, second ed. Kitware Inc..

Jasiuk, I., Chen, J., Thorpe, M.F., 1994. Elastic moduli of two dimensional materials with polygonal elliptical holes. Appl. Mech. Rev. 47 (1), 18–28.

Jolliffe, I.T., 2002. Principal Component Analysis,, .. Series: Springer Series in Statistics, second ed., vol. XXIX. Springer, NY, p. 487.

Kachanov, M., Tsukrov, I., Shafiro, B., 1994. Effective moduli of solids with cavities of various shapes. Appl. Mech. Rev. 47, S151–S174.

Kachanov, M., Shafiro, B., Tsukrov, I., 2003. Handbook of Elasticity Solutions. Kluwer Academic Publishers, Dordrecht.

Kröner, E., 1958. Berechnung der elastischen Konstanten des Vielkristalls aus den Konstanstanten des Einkristalls. Z. Phys. 151, 504–518.

Laraia, V., Rus, I., Heuer, A., 1994. Microstructural shape factors: relation of random planar section to three dimensional microstructures. J. Am. Ceram. Soc. 78, 1532–1536.

Lee, J.K., Johnson, W.C., 1978. Calculation of elastic strain field of a cuboidal precipitate in an anisotropic matrix. Phys. Status Solidi 46, 267–272.

Lin, S., Böhlke, T., Piat, R., Heizmann M., 2010. Determination of correlation functions of pyrolytic carbon microstructures based on an image segmentation technique. In: Proceedings of the IV European Conference on Computational Mechanics – ECCM, Paris, France, 2010.

López-Honorato, E., Meadows, P.J., Shatwell, R.A., Xiao, P., 2010. Characterization of the anisotropy of pyrolytic carbon by Raman spectroscopy. Carbon 48, 881–890.

Markenscoff, X., 1998. Inclusions of uniform eigenstrains and constant or other stress dependence. J. Appl. Mech. 65, 863–866.

McLaughlin, R., 1977. A study of the differential scheme for composite materials. Int. J. Eng. Sci. 15, 237–244.

Mori, T., Tanaka, K., 1973. Average stress in matrix and average energy of materials with misfitting inclusions. Acta Metall. 21, 571–574.

Mura, T., 1987. Micromechanics of Defects in Solids, second ed. Kluwer Academic Publishers.

Nemat-Nasser, S., Hori, M., 1993. Micromechanics: Overall Properties of Heterogeneous Materials. North-Holland.

Nozaki, H., Taya, M., 1997. Elastic fields in a polygon-shaped inclusion with uniform eigenstrain. J. Appl. Mech. 64, 495–502.

Nozaki, H., Taya, M., 2001. Elastic fields in a polyhedral inclusion with uniform eigenstrains and related problems. J. Appl. Mech. 68, 441–452.

Prokopiev, O., Sevostianov, I., 2006. On the possibility of approximation of irregular porous microstructure by isolated spheroidal pores. Int. J. Fract. 139, 129–136.

Piat, R., Tsukrov, I., Böhlke, T., Bronzel, N., Shrinivasa, T., Reznik, B., Gerthsen, D., 2008. Numerical studies of the influence of textural gradients on the local stress concentrations around fibers in carbon/carbon composites. Commun. Numer. Methods Eng. 24, 2194–2205.

Reznik, B., Hüttinger, K.J., 2002. On the terminology for pyrolytic carbon. Carbon 40 (4), 621–624.

Reznik, B., Gerthsen, D., Zhang, W., Hüttinger, K.J., 2003. Texture changes in the matrix of an infiltrated carbon fiber felt studied by polarized light microscopy and selected area electron diffraction. Carbon 41 (2), 376–380.

Rodin, G.J., 1996. Eshelby_s inclusion problem for polygons and polyhedra. J. Mech. Phys. Solids 44, 1977–1995.

Salvo, L., Cloetens, P., Maire, E., Zabler, S., Blandin, J.J., Buffiere, J.Y., Ludwig, W., Boller, E., Bellet, D., Josserond, C., 2003. X-ray micro-tomography an attractive characterisation technique in materials science. Nucl. Instrum. Methods Phys. Res. B 200, 273–286.

Salganik, R.L., 1973. Mechanics of bodies with a large number of cracks. Mech. Solids 4, 149–158 (in Russian).

Sevostianov, I., Kachanov, M., 2002. Explicit cross-property correlations for anisotropic two-phase composite materials. J. Mech. Phys. Solids 50, 253–282.

Sevostianov, I., Kachanov, M., 2007. Relations between compliances of inhomogeneities having the same shape but different elastic constants. Int. J. Eng. Sci. 45, 797–806.

Sevostianov, I., Kachanov, M., 2008. On approximate symmetries of the elastic properties and elliptic orthotropy. Int. J. Solids Struct. 46, 211–223.
Sevostianov, I., Kachanov, M., Zohdi, T., 2008. On computation of the compliance and stiffness contribution tensors of non ellipsoidal inhomogeneities. Int. J. Solids Struct. 45, 4375–4383.
Teng, H., 2010. Stiffness properties of particulate composites containing debonded particles. Int. J. Solids Struct. 47, 2191–2200.
Tsukrov, I., Novak, J., 2002. Effective elastic properties of solids with defects of irregular shapes. Int. J. Solids Struct. 39, 1539–1555.
Tsukrov, I., Drach, B., Gross, T.S., 2009. Influence of anisotropy of pyrolytic carbon on effective properties of carbon/carbon composites. In: Proceedings of the 17th International Conference on Composite Materials – ICCM17, Edinburgh, UK.
Tsukrov, I., Drach, B., 2010. Elastic deformation of composite cylinders with cylindrically orthotropic layers. Int. J. Solids Struct. 47, 25–33.
Wagoner, G., Bacon, R., 1989. Elastic constants and thermal expansion coefficients of various carbon fibers. In: Extended Abstracts of 19th Biennial Carbon Conference, pp. 296–297.
Wu, T.T., 1966. The effect of inclusion shape on the elastic moduli of a two-phase material. Int. J. Solids Struct. 2, 1–8.
Wu, L., Du, S., 1995. The elastic field caused by a circular cylindrical inclusion. J. Appl. Mech. 62, 579–589.
Zimmerman, R.W., 1986. Compressibility of two-dimensional cavities of various shapes. J. Appl. Mech. 53, 500–504.
Zimmerman, R.W., 1991a. Elastic moduli of a solid containing spherical inclusions. Mech. Mater. 12, 17–24.
Zimmerman, R.W., 1991b. Compressibility of Sandstones. Elsevier, Amsterdam.
Zou, W., He, Q., Huang, M., Zheng, Q., 2010. Eshelby's problem of non-elliptical inclusions. J. Mech. Phys. Solids 58, 346–372.